Highlights

Coupled heat and mass transfer in shallow caves: interactions between turbulent convection, gas radiative transfer and moisture transport

B. Qaddah, L. Soucasse, F. Doumenc, S. Mergui, Ph. Rivière, A. Soufiani

- The thermal behavior of a shallow cave presents strong similarities with the simpler academic configuration of the differentially heated cavity.
- Gas radiation increases the flow circulation in the cavity through wall–gas radiative exchanges and significantly modifies the wall radiative flux.
- In the energy balance at the walls, the radiative flux overcomes the conductive flux. However, the addition of conduction and latent heat fluxes, both driven by convection, prevails over radiation in some regions of the cavity.
- The region of the cavity roof at the shortest distance from the ground undergoes the maximum heat and mass fluxes, with condensation resulting in limestone dissolution.

Coupled heat and mass transfer in shallow caves: interactions between turbulent convection, gas radiative transfer and moisture transport

B. Qaddah[a], L. Soucasse[a], F. Doumenc[b,c], S. Mergui[b,c], Ph. Rivière[a], A. Soufiani[a]

[a] *Laboratoire EM2C, CNRS, CentraleSupélec, Université Paris-Saclay, 8-10 rue Joliot Curie, 91192 Gif-sur-Yvette, France*
[b] *Universitée Paris-Saclay, CNRS, FAST, 91405, Orsay, France*
[c] *Sorbonne Universitée, UFR 919, 4 place Jussieu, F-75252, Paris Cedex 05, France*

Abstract

Understanding and predicting the microclimate of shallow caves is a key issue for the conservation of parietal art. In order to determine the dominant mechanisms of heat transfer in a configuration close to that of painted caves, we performed numerical simulations of a parallelepiped cavity whose dimensions and depth are of the order of 10 m. This simple geometry allowed us to use a detailed model including turbulent natural convection, gas radiation, along with vapor transport and latent heat fluxes resulting from condensation and evaporation on the walls.

Gas radiation increases the flow circulation in the cavity through wall–gas radiative exchanges and significantly modifies the wall radiative flux. Conversely, the wall conductive flux remains unchanged (a non trivial behavior reported in the literature about the differentially heated cavity). In the energy balance at the walls, the radiative flux overcomes the conductive flux. However, the addition of conduction and latent heat fluxes, both driven by convection, prevails over radiation in some regions of the cavity.

Heat and mass fluxes are maximum in areas of the cavity roof where the distance from the ground is the shortest. Due to the asymmetry induced by the inversion of the vertical temperature gradient twice a year, net condensation resulting in limestone dissolution is expected in these areas, whereas

Email address: doumenc@fast.u-psud.fr (F. Doumenc)

the other regions of the cave undergo net evaporation resulting in limestone deposition. The orders of magnitude of the condensation flux (a few microns per day) and of the retreat velocity of the wall (a few tenth of a micron per year) are in line with the field data available in the literature.

Keywords: Shallow caves, Heat and mass transfer, Turbulent natural convection, Gas radiation, Condensation, Corrosion

1. Introduction

Predicting cave microclimate is essential in many fields as diverse as paleoclimate reconstruction [1], tunneling [2], or the study of subterranean fauna and flora [3]. This is also a critical issue for the conservation of cave paintings. Indeed, the exceptional state of conservation of parietal prehistoric paintings is mainly due to the high stability of cave microclimate. However, cave microclimate can be disturbed in various ways. A visitor influx results in a sudden increase of temperature, carbon dioxide (CO_2) concentration and humidity [4, 5, 6]. Cave modifications required to accommodate visitors (artificial ventilation [5], creation of a large entrance [7], removal of a detritic scree acting as a thermal buffer [8]) may increase heat and mass exchanges with the external environment. The potential consequences of these disturbances are manifold. The microbiological balance can be disturbed, resulting in the formation of stains on the walls [9]. CO_2 fluctuations may result in the corrosion of limestone walls by dissolution of calcium carbonate ($CaCO_3$) or, conversely, deposition of $CaCO_3$ films. $CaCO_3$ dissolution or deposition can also be triggered by condensation and evaporation [10, 11, 12]. Moreover, condensation is at the core of other issues. First, it can increase the risk of growth of unwanted microbiological species as fungi [13, 14]. Second, the possibility to form vermiculations by water condensation was recently demonstrated through laboratory experiments [15]. Vermiculations are natural patterns commonly observed on cave walls [16]. The formation of vermiculations in painted caves triggers the migration of painting pigments along the wall [17], resulting in serious damages to the paintings [18].

A deep understanding of heat transfer within the cave and between the cave and the external environment is thus required for a rational management of painted caves and to achieve proper remediation when it becomes necessary (e.g., by designing and building artificial thermal buffers [8]). In this article we focus on closed shallow caves, i.e., caves with negligible air ex-

changes with the external environment and located at depths ranging from a few meters to 20 m. Many painted caves fall in this category, including the famous Lascaux Cave in France [7] and Altamira Cave in Spain [19]. For such caves, heat transfer between the ground level and the cave is mainly due to heat conduction [20, 19], while natural convection and infrared radiation occur inside the cave. In the range of depth considered here, daily temperature fluctuations are completely damped by heat diffusion in the rock layer between the ground level and the cave, but yearly fluctuations are still measurable. Due to the complex geometry of the cave and depth variations all along the cave, spatial temperature differences at a given time are also expected. For instance, the amplitude of the yearly temperature variations in the Hall of Bull in Lascaux Cave is of the order of a few tenth of degrees [21, 22]. The spatial temperature variations at a given time inside the cave are of the same order [23].

Such temperature variations might seem very small. However, in a cave of 5 m height with a temperature difference of 0.1 K between the floor and the roof, the Rayleigh number is of the order of 10^9, value at which turbulent natural convection is expected. This was confirmed through the resolution of Navier–Stokes equations based on large eddy simulations (LES) [24], a method which allows the accurate prediction of the turbulent flow structure. In this recent work, we considered the case of a parallelepiped cavity whose size and depth roughly mimic the dimensions of the Hall of Bull in Lascaux Cave. Assuming that the cave atmosphere was dry (no release of latent heat) and transparent to the infrared radiation, we compared the wall convective and radiative heat fluxes. We showed that, with the assumptions mentioned above, wall-to-wall radiation was the dominant mechanism. But the real situation is further complicated by two factors typical of cave atmospheres.

1. In weakly ventilated caves, the natural infiltration of water through the pores and the fissures of the rock results in relative humidity close to 100% [19, 8]. Under these conditions, small temperature differences are sufficient to produce significant evaporation and condensation fluxes, resulting in latent heat release on the walls and vapor transfer from the hot to the cold spots of the cave.
2. The amount of CO_2 in soils is controlled by plant roots, microorganisms respiration and organic matter decomposition [25]. The CO_2 is transferred from soils to caves in gaseous form or after dissolution in water. Whereas the molar fraction of CO_2 in the atmosphere is ap-

proximately 0.04%, it can reach several percent in caves [21]. Due to the presence of saturated water vapor and CO_2, the cave atmosphere should probably not be considered as transparent for the infrared radiation. Indeed, the emission and absorption of radiation affect the temperature of a radiating fluid, which in turn controls the buoyant motion. Gas radiation has been shown to significantly interact with convection in various configurations including plumes generated by a localized heat source [26], the Rayleigh–Bénard cell [27] or the differentially heated cavity [28, 29]. Among the academic configurations studied in the literature, the latter is the closest to ours. It consists of two vertical, parallel, isothermal walls surrounded by four adiabatic walls. Soucasse *et al* [30, 31] and Kogawa *et al* [32, 33] simulated the turbulent natural convection coupled to wall and gas radiation in a differentially heated cubical cavity. The cavity was filled with a mixture of air, water vapor and CO_2. These authors observed that wall-gas radiative exchanges induced a thickening of vertical boundary layers resulting in a strong intensification of the global circulation in the cavity and an increase of the turbulence level. However, conductive fluxes through the walls were little modified by gas radiation. Soucasse *et al* worked at Rayleigh numbers ranging from $\mathrm{Ra} = 3 \times 10^7$ to 3×10^9. The averaged transmissivity based on the cavity size and weighted by the Planck function at room temperature was equal to 0.83. The study of Kogawa *et al* [32, 33] was performed at Rayleigh number 1.5×10^9 with different concentrations of water vapor and CO_2 corresponding to transmissivities of 0.89 and 0.64. They found results similar to those of Soucasse *et al* (enhancement of the global circulation with little effect on the wall conductive fluxes).

The temperature field inside a cave thus results from a complex interplay between heat conduction in the surrounding rock and, inside the cave, turbulent natural convection resulting in heat and mass convective transfer, heat conduction and latent heat release on the walls, and radiative transfer between the cave walls and between the cave walls and the cave atmosphere. All of these mechanisms are strongly coupled. The main objective of the present article is to assess their relative significance, determine those that are dominant, and those that can be neglected with no significant loss of accuracy. For this purpose, we rely on the same approach as already implemented in ref. [24], but we now consider that the cave atmosphere is humid and radiant.

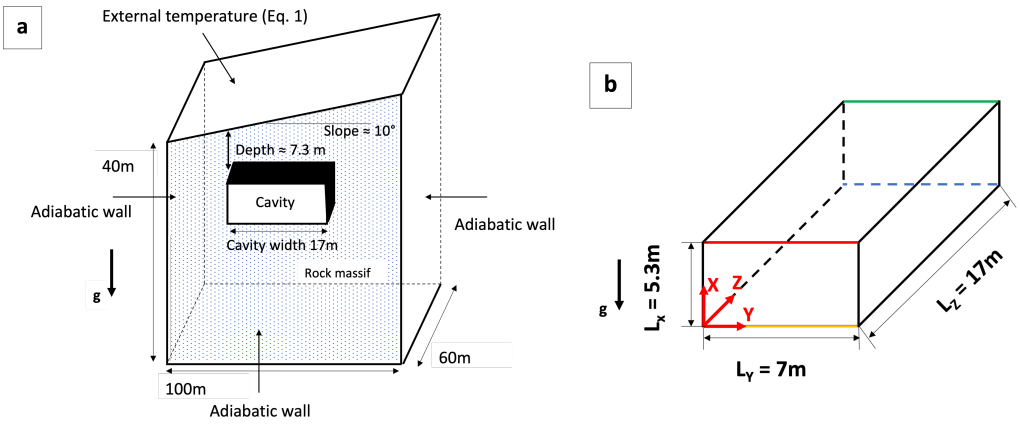

Figure 1: a) General geometry of the rock mass (not at scale). b) Detailed diagram of the cavity, with the definition of the axes. Red, yellow, green and blue lines correspond to the left upper ($Z = 0$ and $X = L_X$), left bottom ($Z = 0$ and $X = 0$), right upper ($Z = L_Z$ and $X = L_X$) and right bottom ($Z = L_Z$ and $X = 0$) edges, respectively

Numerical simulations are performed in the simplified case of a parallelepiped cavity, which allows the use of an accurate mathematical model in which the coupling between radiative transfer and convective heat and mass transports inside the cavity are strictly implemented. This approach provides the orders of magnitude of the various heat and mass fluxes through the cave walls, including the time and location of condensation events. Simplifications to be made in future models of closed shallow caves are deduced from these results.

The article is organized as follows. The problem statement and the physical assumptions used in the model are detailed in Sec. 2. The governing equations and the numerical methods are presented in sections 3 and 4. Section 5 describes the effects of the solutal buoyancy and the gas radiation on the flow pattern. The consequences on heat and mass fluxes through the cavity walls are reported in Sec. 6.

2. Problem statement

2.1. Geometry and boundary conditions

We consider the same confined parallelepiped cavity as in our previous work [24]. The cavity is embedded in the rock mass displayed in Fig. 1a. The ground surface is inclined at 10° from the horizontal direction. Its tem-

perature follows the external temperature

$$T_{ex}(t) = T_m + A\cos\left(2\pi\frac{t}{\tau}\right) , \tag{1}$$

where $\tau = 1\,\text{year}$ is the period, $T_m = 12°\text{C}$ is the annual average external temperature and $A = 8°\text{C}$ is the amplitude of the temperature variations (these values of T_m and A are typical of the climate conditions in south–west of France). As we only consider the periodic regime, we arbitrarily assume that the initial time corresponds to the hottest temperature of the year that takes place in July. The other external boundaries of the rock mass are all adiabatic. The left upper edge of the cavity is located at a depth of 7.3 m. The cave dimensions are the height $L_X = 5.3\,\text{m}$, the width $L_Y = 7\,\text{m}$ and the length $L_Z = 17\,\text{m}$. The axes $\boldsymbol{X}$, $\boldsymbol{Y}$ and $\boldsymbol{Z}$ are displayed in Fig. 1b. $\boldsymbol{g} = -g\boldsymbol{X}$ is the gravitational acceleration field.

Ideally, we should consider a 1–year periodic problem including heat conduction in the rock fully coupled with radiation and turbulent natural convection inside the cave. However, a one–year simulation of the Navier–Stokes equations in the turbulent regime is not practicable with current computational resources. In our previous work [24], this difficulty was overcome by defining a large–scale model including heat conduction in the rock and radiative transfer between the cavity walls, but disregarding natural convection inside the cavity. Solving the 1–year periodic regime of this large–scale model yielded temperature fields of the cavity walls throughout the year (see the results for May and November in Fig. 2). In a second step, these wall temperature fields at six selected times of the year were used as boundary conditions to solve the natural convection problem inside the cavity (Chebyshev pseudo–spectral method associated to large eddy simulations (LES) with a spectral vanishing viscosity (SVV) model). The Rayleigh number $Ra = g\beta_T\Delta T L_X^3/(\alpha\nu)$ was based on the difference ΔT between the maximum and the minimum wall temperatures (with g the gravity acceleration, β_T the thermal expansion coefficient, α the thermal diffusivity and ν the kinematic viscosity). Ra ranged from 2.1×10^9 (in August and February) to 8.4×10^9 (in May and November). Two flow regimes were identified. A one–cell flow regime with a large level of turbulence and an isothermal core (strong thermal mixing) was observed when the vertical gradient was negative (roof colder than the floor). This happened in March, May and August. Conversely, a multiple-cell flow regime with a lower turbulence level and a thermal stratification in the core was observed when the vertical gradient

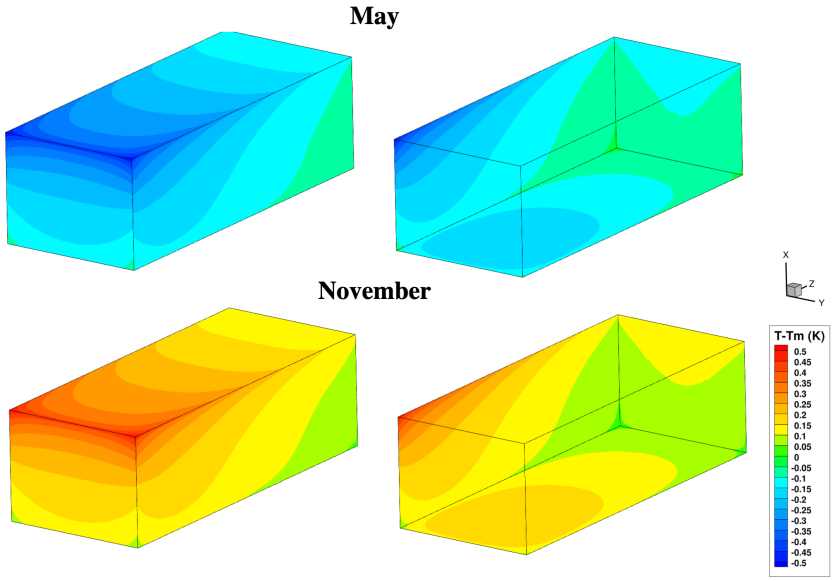

Figure 2: Wall temperature fields $T - T_m$ computed from the large-scale model for May and November (from ref. [24]). The left panel corresponds to the top ($X = L_X$), left ($Z = 0$) and front ($Y = L_Y$) cave walls. The right panel corresponds to the bottom ($X = 0$), right ($Z = L_Z$) and rear ($Y = 0$) cave walls. The difference ΔT between the maximum and the minimum wall temperatures is 0.492 K in both cases.

was positive, in September, November and February. In both regimes, heat transfer at the cavity walls was dominated by the radiative flux. This *a posteriori* justified that natural convection was neglected in the determination of the thermal boundary conditions at the cave walls by the large–scale model.

We follow the same approach in the present work to determine the effect of vapor transfer and gas radiation. We assume that the large-scale model provides realistic temperature distributions on cave walls, and we use them as boundary conditions. The natural convection problem, including heat and mass transfer coupled to radiation, is solved by LES with the SVV model. We focus on May and November, both months associated with the largest temperature gradients, as typical of the one-cell flow regime and the multiple-cell flow regime, respectively. The physical assumptions needed to model the mass transfer and the gas radiation are detailed in sections 2.2 and 2.3 below.

2.2. Mass transfer, condensation and evaporation

The density of the cave atmosphere mainly depends on three parameters: the temperature, the water vapor concentration and the CO_2 concentration. Therefore, the gradient of each of these three quantities may contribute to the buoyancy that drives natural convection. However, the dynamics of the CO_2 is an intricate problem. Several mechanisms with different time scales may be responsible for the transfer of CO_2 from the soil to the cave [34, 23]. As a first step, uniform CO_2 concentration will be considered in the present work. We thus assume that the buoyancy is only due to the gradients of temperature and water vapor concentration. The resulting thermal and solutal buoyant forces add up since the water vapor content increases with temperature and water vapor is lighter than dry air. The relative contributions of these two factors will be assessed.

We investigate the case of cave walls entirely covered with a thin water film whose origin may be percolation and/or condensation. In general, condensation may also occur in the gas phase, resulting in the formation of clouds. Clouds have been observed in caves, in certain configurations (e.g., the mixing of two air streams at different temperatures [35]). However, aerosols acting as nucleation points are necessary to initiate the formation of droplets. The presence of such aerosols in caves is strongly correlated to the ventilation and the visitor disruptions [36]. In weakly ventilated caves with a reduced number of visitors, the presence of significant aerosols lasting on long times is unlikely. We thus disregard condensation in the gas phase, and we assume that evaporation and condensation take place on the walls only.

The high dilution of the water vapor in the cave atmosphere allows to simplify the derivation of the condensation/evaporation flux at the cave wall. Indeed, the saturated vapor pressure $P_{sat} \simeq 14.03\,\mathrm{mbar}$ at temperature $T_m = 12°\mathrm{C}$ [22] and the atmospheric pressure $P_{atm} \simeq 1013\,\mathrm{mbar}$ yield the water vapor molar fraction $x_w \simeq P_{sat}(T_m)/P_{atm} \simeq 0.014$, much lower than 1. In such a situation, the condensation or evaporation fluxes are driven by the diffusion of the dilute vapor through the non-condensable gases (air and CO_2 in our case). The kinetic resistance at the liquid–gas interface can be neglected compared to the transfer resistance of the solutal boundary layer in the gas phase, and the local thermodynamic equilibrium is assumed at the liquid–gas interface (see for instance Ref. [37] for a detailed discussion on the physical mechanisms driving evaporation or condensation). Therefore, the water vapor is always saturated at the walls, and can be slightly undersaturated or supersaturated in the core of the gas phase. In the simulation

results, the volume–averaged absolute value of the deviation from saturation was always lower than 10^{-3}.

2.3. Radiative properties of the cave atmosphere

With the assumption of a clean atmosphere, there is no scattering due to suspended particles. The radiative properties of the cave atmosphere thus reduce to the absorption coefficient κ_ν, which depends on the radiation wavenumber ν and the atmosphere composition. Fig. 3 shows the absorption spectrum of air mixed with CO_2 and water vapor at molar fractions $x_{CO_2} = 0.02$ and $x_w = 0.014$, respectively. The temperature is the yearly averaged atmospheric temperature $T_m = 285.15\,\mathrm{K}$ and the total pressure is $P_{atm} = 1\,\mathrm{atm}$. The molar fraction of water vapor corresponds to saturated vapor at temperature T_m. The absorption spectrum was calculated from a line by line approach using the HITRAN database [38].

The significance of gas radiation compared to wall radiation can be estimated from the transmissivity τ_g defined as

$$\tau_g = \frac{\pi}{4\sigma_{SB}T_m^3}\int_\nu \exp(-\kappa_\nu \ell)\frac{dI_\nu^0}{dT}(T_m)d\nu\,, \qquad (2)$$

where σ_{SB} and $I_\nu^0(T_m)$ are the Stefan–Boltzmann constant and the Planck function, respectively. The transmissivity τ_g is the net radiative flux exchanged by two black walls through an optical path of mean beam length ℓ, scaled by the net radiative flux through a transparent medium (the radiative transfer temperature dependence has been linearized). The relative contribution of gas radiation compared to surface–to–surface radiation is expected to be negligible for $\tau_g \simeq 1$ and dominant for $\tau_g \ll 1$.

τ_g is displayed in Fig. 4 for the three values $x_{CO_2} = 0, 0.02$ and 0.1, at constant water vapor molar fraction $x_w = 0.014$. A rough estimation of the transmissivity between two opposite walls of the cave can be obtained from Fig. 4 assuming a characteristic size of 10 m (the order of magnitude of the cavity size, see Fig. 1). The corresponding transmissivity decreases from 0.81 to 0.66 when the CO_2 molar fraction increases from 0 to 0.1. These values suggest a non negligible contribution of gas radiation to the radiative transfer. Furthermore, the results obtained by Soucasse *et al* [30, 31] and Kogawa *et al* [32, 33] for the differentially heated cavity with similar Rayleigh numbers and transmissivities (see Sec. 1) also suggest a significant modification of the flow pattern by gas radiation. Figure 4 indicates an increase of these two

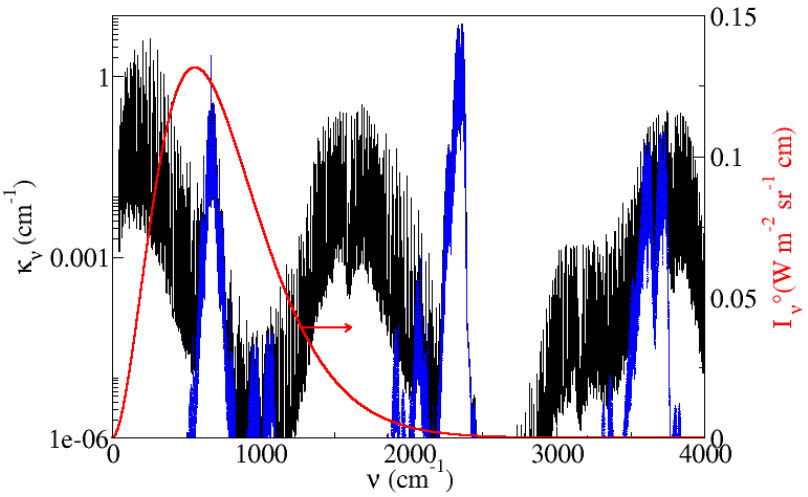

Figure 3: Absorption coefficient spectrum of the cave atmosphere considered as a mixture of air, saturated water vapor (molar fraction $x_w = 0.014$) and CO_2 (molar fraction $x_{CO_2} = 0.02$) at temperature $T_m = 285.15\,\mathrm{K}$ and atmospheric pressure (black); CO_2 contribution (blue); Planck function $I^\circ_\nu(T_m)$ (red).

effects (contribution of gas radiation to radiative transfer and modification of the flow pattern) with the CO_2 level. In the following, we set $x_{CO_2} = 0.02$, a high level of CO_2 commonly observed in caves. The corresponding value of τ_g is approximately 0.7.

3. Governing equations

3.1. Natural convection

In the parallelepiped cavity displayed in Fig. 1b, we consider the natural convection flow of a humid air mixture caused by both temperature and moisture gradients. Conservation equations for mass, momentum, energy and water vapor concentration write

$$\boldsymbol{\nabla} \cdot \boldsymbol{u} = 0, \tag{3}$$

$$\frac{\partial \boldsymbol{u}}{\partial t} + \boldsymbol{u} \cdot \boldsymbol{\nabla} \boldsymbol{u} = -\frac{1}{\rho_0} \boldsymbol{\nabla} p + \beta_T (T_0 - T) \boldsymbol{g} + \beta_c (c_0 - c) \boldsymbol{g} + \nu \boldsymbol{\nabla}^2 \boldsymbol{u}, \tag{4}$$

$$\frac{\partial T}{\partial t} + \boldsymbol{u} \cdot \boldsymbol{\nabla} T = \alpha \boldsymbol{\nabla}^2 T + \frac{1}{\rho_0 C_P} \mathcal{P}_{\mathrm{rad}}, \tag{5}$$

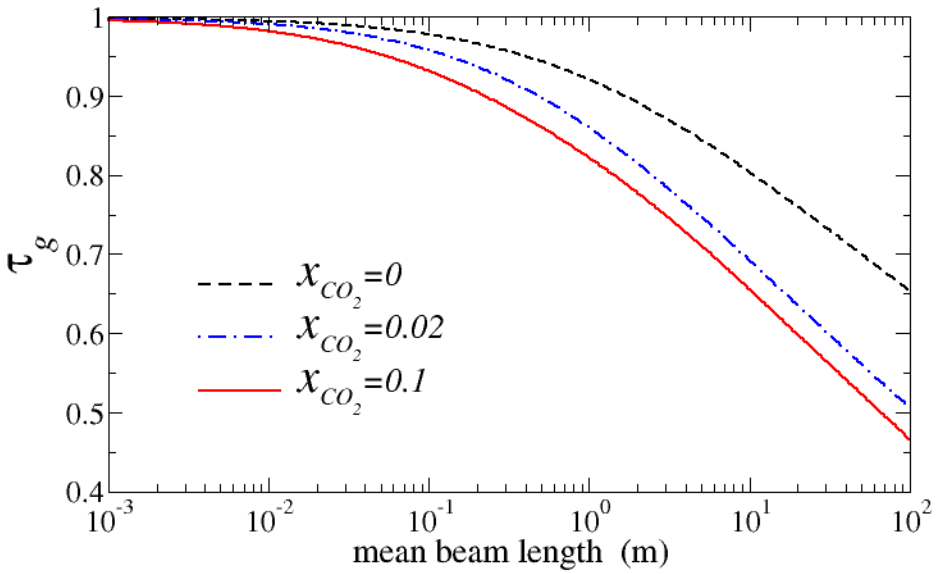

Figure 4: Effect of the CO_2 concentration on the transmissivity τ_g defined in Eq. (2) as a function of the mean beam length ℓ, at temperature $T_m = 285.15\,\mathrm{K}$ and atmospheric pressure, for saturated water vapor (molar fraction $x_w = 0.014$).

$$\frac{\partial c}{\partial t} + \boldsymbol{u} \cdot \boldsymbol{\nabla} c = D \boldsymbol{\nabla}^2 c, \tag{6}$$

where $\boldsymbol{u}$, p, T and c are respectively the velocity vector, the motion pressure, the temperature, and the water vapor mass concentration. The radiative power $\mathcal{P}_{\text{rad}}$ in the energy balance (Eq. (5)) corresponds to the emission and absorption of radiation by the fluid and will be discussed in details in Sec. 3.2. There is no source term due to phase change in transport equations (5)-(6) because phase change is supposed to take place on the walls only (see section 2.2). It should be noted here that subgrid terms complement Eqs. (4)-(6) when the LES approach is employed (see Sec. 4.1).

The boundary conditions at the cave walls are defined as follows. We assume that the water film lying on the walls is thin enough to neglect: (1) its velocity compared to the air velocity, (2) its conductive thermal resistance compared to the boundary layer resistance in the gas phase. With the additional assumptions of no slip and local thermodynamic equilibrium on the walls, we get:

$$\boldsymbol{u} = \boldsymbol{0}, \quad T = T_w \quad \text{and} \quad c = c_{sat}(T_w)\,, \tag{7}$$

where T_w is the wall temperature given by the large scale model (see Sec. 2.1 and Fig. 2), and $c_{sat}(T_w)$ is the concentration of the saturated water vapor at temperature T_w. Because of the small temperature range considered in the simulations (approximately 1 K), we assume that $c_{sat}(T)$ varies linearly with the temperature T [22]:

$$c_{sat}(T) = c_{sat}(T_m) + \beta(T - T_m)\,, \tag{8}$$

where β is the derivative of $c_{sat}(T)$ at $T = T_m$ (see table 1).

The physical properties of the fluid are listed in table 1. Following the Boussinesq approximation, the fluid density is assumed constant except in the buoyancy term of the momentum balance (Eq. (4)), where it varies linearly with temperature and moisture content. The reference temperature is $T_0 = [\max(T_w) + \min(T_w)]/2$. Similarly, the reference concentration of water vapor is $c_0 = [\max(c_{sat}(T_w)) + \min(c_{sat}(T_w))]/2$.

3.2. Radiative transfer

The radiative power $\mathcal{P}_{\text{rad}}$ in the energy balance (Eq. (5)) is defined by

$$\mathcal{P}_{\text{rad}}(\boldsymbol{r}) = \int_{\nu} \kappa_\nu \left(\int_{4\pi} I_\nu(\boldsymbol{r}, \boldsymbol{\Omega})\, d\boldsymbol{\Omega} - 4\pi I^\circ_\nu(T(\boldsymbol{r})) \right) d\nu, \tag{9}$$

where $I_\nu(\boldsymbol{r}, \boldsymbol{\Omega})$ is the radiative intensity at wavenumber ν, position $\boldsymbol{r}$, and direction $\boldsymbol{\Omega}$, $d\boldsymbol{\Omega}$ is the differential solid angle and $I^\circ_\nu(T(\boldsymbol{r}))$ is the Planck equilibrium intensity (blackbody intensity) at temperature T. The absorption coefficient κ_ν is assumed to be uniform.

The radiative intensity satisfies the radiative transfer equation

$$\boldsymbol{\Omega} \cdot \boldsymbol{\nabla} I_\nu(\boldsymbol{r}, \boldsymbol{\Omega}) = \kappa_\nu \left(I^\circ_\nu(T(\boldsymbol{r})) - I_\nu(\boldsymbol{r}, \boldsymbol{\Omega}) \right). \tag{10}$$

Cave walls are assumed to be black (the emissivities of limestone and water are respectively equal to 0.95 and 0.96 [39], thus close to 1 in both cases). Therefore, the boundary condition for Eq. (10) at wall positions $\boldsymbol{r}^b$ for the propagation directions $\boldsymbol{\Omega}$ such that $\boldsymbol{\Omega} \cdot \boldsymbol{n} > 0$, $\boldsymbol{n}$ being the unit vector normal to the wall pointing to the interior of the domain, writes $I_\nu(\boldsymbol{r}^b, \boldsymbol{\Omega}) = I^\circ_\nu(T(\boldsymbol{r}^b))$.

The annual variations of gas temperature and water vapor molar fraction are not large enough to significantly affect the radiative properties of the mixture. Indeed, the amplitude of temperature fluctuations during the year is approximately $\pm 1\,\mathrm{K}$. Assuming saturated water vapor, the corresponding annual fluctuation of x_w is smaller than $\pm 7\,\%$. These fluctuations of temperature and water vapor concentration result in variations of the absorption coefficient κ_ν lower than $7\,\%$. The constant absorption spectrum displayed in Fig. 3 was thus used in all simulations.

3.3. Heat and mass fluxes through the cave wall

The distribution of the evaporation and heat fluxes through the cave wall are among the most important outputs of the model. The evaporation velocity (i.e., the volume of evaporated liquid water per unit of surface and time) reads:

$$v_{ev} = -\frac{D}{\rho_w} \boldsymbol{\nabla} c \,.\boldsymbol{n}\,, \tag{11}$$

where ρ_w is the density of liquid water. v_{ev} is positive for evaporation and negative for condensation (the normal vector $\boldsymbol{n}$ is directed towards the cavity).

The total heat flux q_{th} through the cave wall is the sum of the conduction flux q_{con}, the latent heat flux q_{lat} and the radiative flux q_{rad}:

$$q_{th} = \underbrace{-\lambda \boldsymbol{\nabla} T \,.\boldsymbol{n}}_{q_{con}} + \underbrace{\mathcal{L} \rho_w v_{ev}}_{q_{lat}} + \underbrace{\int_\nu \int_{4\pi} I_\nu(\boldsymbol{r}^b, \boldsymbol{\Omega})\, \boldsymbol{\Omega} \cdot \boldsymbol{n}\, d\boldsymbol{\Omega}\, d\nu}_{q_{rad}}, \tag{12}$$

Physical property	Name	Numerical value
Air density	ρ_0	$1.23\,\mathrm{kg.m^{-3}}$
Kinematic diffusivity	ν	$1.46 \times 10^{-5}\,\mathrm{m^2.s^{-1}}$
Specific heat	C_p	$1.005 \times 10^3\,\mathrm{J.kg^{-1}.K^{-1}}$
Thermal conductivity	λ	$0.025\,\mathrm{W.m^{-1}.K^{-1}}$
Thermal diffusivity	α	$2.05 \times 10^{-5}\,\mathrm{m^2.s^{-1}}$
Water latent heat of vaporization	$\mathcal{L}$	$2.473 \times 10^6\,\mathrm{J.kg^{-1}}$
Thermal expansion coefficient	β_T	$3.51 \times 10^{-3}\,\mathrm{K^{-1}}$
Solutal expansion coefficient	β_c	$0.490\,\mathrm{m^3.kg^{-1}}$
Saturated vapor concentration	$c_{sat}(T_m)$	$1.065 \times 10^{-2}\,\mathrm{kg.m^{-3}}$
Derivative of $c_{sat}(T)$	$\beta = c'_{sat}(T_m)$	$7.03\ \times 10^{-4}\,\mathrm{kg.m^{-3}.K^{-1}}$
Water/vapor solutal diffusivity	D	$2.43 \times 10^{-5}\,\mathrm{m^2.s^{-1}}$
Prandtl number	$\mathrm{Pr} = \nu/\alpha$	0.712
Schmidt number	$\mathrm{Sc} = \nu/D$	0.601
Lewis number	$\mathrm{Le} = \alpha/D$	0.844

Table 1: Physical properties of the cave atmosphere at temperature $T_m = 285.15\,\mathrm{K} \simeq 12\,^\circ\mathrm{C}$ (from ref. [22]).

where $I_\nu(\boldsymbol{r}^b, \boldsymbol{\Omega})$ is the radiative intensity at the cave wall. Equation (12) allows to estimate the relative contribution of each heat transfer mechanism to the total heat flux through the cave wall.

4. Numerical methods

4.1. Natural convection

Flow equations (3)-(6) are solved using a Chebyshev collocation method [40]. Domain decomposition along the horizontal direction is carried out by the Schur complement method to make the computations parallel [41]. Time integration is performed through a second-order semi-implicit scheme. The velocity divergence-free condition is enforced using a projection method.

The large-eddy simulation (LES) approach is used in this study to save computational time. The Spectral Vanishing Viscosity (SVV) method [42, 43, 44] is employed to model the effects of the unresolved subgrid scales, because it is particularly suitable for spectral methods. It consists in introducing an artificial dissipation term to ensure spectral convergence and dissipate the high modes of the Chebyshev polynomial development. The SVV method is

implemented in the form of a modified Laplacian operator $\boldsymbol{\nabla}^2_{SVV}$ combining viscous and SVV dissipation such that

$$\boldsymbol{\nabla}^2_{SVV} = \boldsymbol{\nabla} \cdot (1 + \nu^{-1} Q) \boldsymbol{\nabla}, \tag{13}$$

for the momentum balance. For the energy balance and the water vapor balance, the same operator is used with the thermal diffusivity α and the mass diffusivity D instead of the kinematic viscosity ν in Eq. (13). The viscosity kernel Q acts on each spatial direction independently. In spectral space, it is given for the i^{th} direction by $\hat{Q}_i(k) = \epsilon_i e^{-\left(\frac{k-N_i}{k-M_i}\right)^2}$, if $k > M_i$ or $\hat{Q}_i(k) = 0$ otherwise, where k is the Chebyshev polynomial order, ϵ_i is the viscosity amplitude, N_i is the number of collocation point in the i^{th} direction and $M_i \leqslant N_i$ is the cut-off spectral mode. ϵ_i and M_i are the control parameters of the SVV method. The numerical modeling reduces by either increasing M_i or decreasing ϵ_i. It is worth noting that the same SVV parameters are used in the momentum balance, in the energy balance and in the water vapor balance.

Simulations have been carried out using a spatial mesh made of $N_x \times N_y \times N_z = 241 \times 241 \times 641$ collocation points. SVV parameters are chosen such that $M_i = 3N_i/4$ and $\epsilon_i = 1/(4N_i)$ for each spatial direction i. Time integration is performed with a convection time step $\delta t = 0.001 \times t_{\text{ref}}$, where $t_{\text{ref}} \simeq 15\ s$ is the reference time associated with the reference length L_X and the reference velocity $\sqrt{g\beta_T \Delta T L_X / Pr}$. In Sec. 5, results will be analyzed in terms of time-averaged quantities over a time period $\Delta t = 100 \times t_{\text{ref}}$, taken once the statistically steady state is reached.

4.2. Radiative transfer

The high resolution spectrum of the absorption coefficient displayed in Fig. 3 contains thousands of spectral lines which makes expensive the computation of the integral over the wavenumbers in Eq. (9). Therefore, we use the Absorption Distribution Function (ADF) model [45] which consists in substituting the integration over the wavenumber with an integration over the values of the absorption coefficient, for which a coarse logarithmic discretization is sufficient. In the present study, the values of the absorption coefficient of Fig. 3 have been logarithmically discretized in 16 classes. The accuracy of this method has been shown to be better than 1 % [46].

The radiative transfer equation (10) is solved using a ray-tracing algorithm for each ADF class of absorption coefficient value. The computation

is made parallel by distributing the rays among the different processors. The 4π angular domain is uniformly discretized using 900 rays from volume cell centers and 450 rays from boundary cell centers. The radiation mesh is coarsened by a factor of five in each direction of space compared with the convection mesh and we use a radiation subgrid model [47] to account for the radiation of the spatial scales resolved by the flow mesh but filtered by the coarse radiation mesh. The radiation of spatial scales unresolved by the flow mesh is ignored. This subgrid model has been validated in various configurations and its accuracy is approximately a few per cent on radiative power and wall fluxes. It has been used for the simulation of coupled natural convection and radiation in differentially heated cavities [31] and Rayleigh-Bénard cells [48].

Finally, an explicit coupling is carried out between flow and radiation calculations and the radiative power is updated every 10 convection time steps δt. Indeed, the flow time step is imposed by numerical stability constraints and does not correspond to significant variations of the temperature field.

4.3. Validation

We first compare in this section Direct Numerical Simulations (DNS) to some experimental data available in the literature. We then validate the LES approach through comparisons with DNS results in the shallow cave configuration.

Figure 5 shows comparisons between DNS and experimental data for Rayleigh-Bénard convection in cubical cavities. The DNS data correspond to isothermal horizontal walls, adiabatic side-walls, dry and non-radiating air. The data were obtained with the same code and numerical setup used in the present study, and were already presented in Ref. [27]. Both experiments and numerical simulations are related to gases with a Prandtl number close to 0.7. In the experiment carried out by Belmonte *et al* [56], the cubical convection cell was put under pressure inside a cylindrical external vessel. The volume between both cavities was filled by cotton batting in order to impede any external motion and to increase thermal insulation of the cavity lateral side-walls. The authors have measured the Nusselt number at the center of the horizontal isothermal plates but they concluded that this value is representative of the average Nusselt number on the surface of the plate. On the opposite, Leong *et al* [57] have considered highly conducting side lateral walls, leading to less uncertain boundary conditions with a nearly linear temperature profile along the vertical axis for these side-walls. The

comparisons presented in Fig. 5 show a good agreement between numerical results and experimental data, despite the differences in side-wall boundary conditions.

In addition, Leong *et al* [57] carried out experiments with differentially heated cubical cavities, i.e. two vertical and opposite active walls with conducting walls for the four remaining side-walls. They provided a correlation for this case in the form $\mathrm{Nu} = 0.08461\,\mathrm{Ra}^{0.3125}$ for $10^4 \leq \mathrm{Ra} \leq 10^8$. DNS with the same boundary conditions on the side-walls led to $\mathrm{Nu} = 35.73$ at $\mathrm{Ra} = 3 \times 10^8$ [58]. A slight extrapolation of the experimental correlation yields $\mathrm{Nu} = 37.72$, which is in quite satisfactory agreement.

In a second step, the Spectral Vanishing Viscosity (SVV) model has been validated against DNS data in the case of a dry and transparent gas (C case in Table 3) for the month of February. Table 2 reports LES and DNS results for macroscopic quantities such as the volume-averaged reduced mean temperature ($\theta = (T - T_0)/\Delta T$), the volume-averaged dimensionless kinetic energy of the mean flow, the volume-averaged dimensionless turbulent kinetic energy, and the Nusselt number $\overline{Nu} = \bar{q}_{con} L_X/(\lambda \Delta T)$ where $\bar{q}_{con}$ is the conduction flux averaged at the upper ($X = L_X$), left ($Z = 0$) or side ($Y = 0$) walls. Two meshes (LES_{240} using $241 \times 241 \times 641$ points and LES_{160} using $161 \times 161 \times 641$ points) and two sets of SVV parameters M and ϵ are considered to assess the sensitivity of the LES results. The DNS mesh is made of $321 \times 321 \times 1025$ points. The best agreement is obtained for the LES parameters retained for the coupled simulations (LES_{240} mesh, $M = 3N/4$, $\epsilon = 1/(4N)$) with differences with DNS results below 10 %. This maximum difference is observed for the turbulent kinetic energy. The accuracy of the LES decreases with the coarser LES_{160} mesh (differences with DNS up to 20 %) but is little affected by the change in SVV parameters M and ϵ. More details on this validation can be found in Ref. [24].

5. Flow field analysis

5.1. The studied configurations

In order to highlight specific effects associated with gas radiation and solutal buoyancy, numerical simulations were performed with different versions of the model described in Sec. 3. We considered three cases, labelled C, CR and CRM (see Tab. 3). The CRM model is the full model used as a reference. It includes gas radiation and the contribution of the water vapor concentration field to buoyancy. In the CR model, the contribution of the water vapor

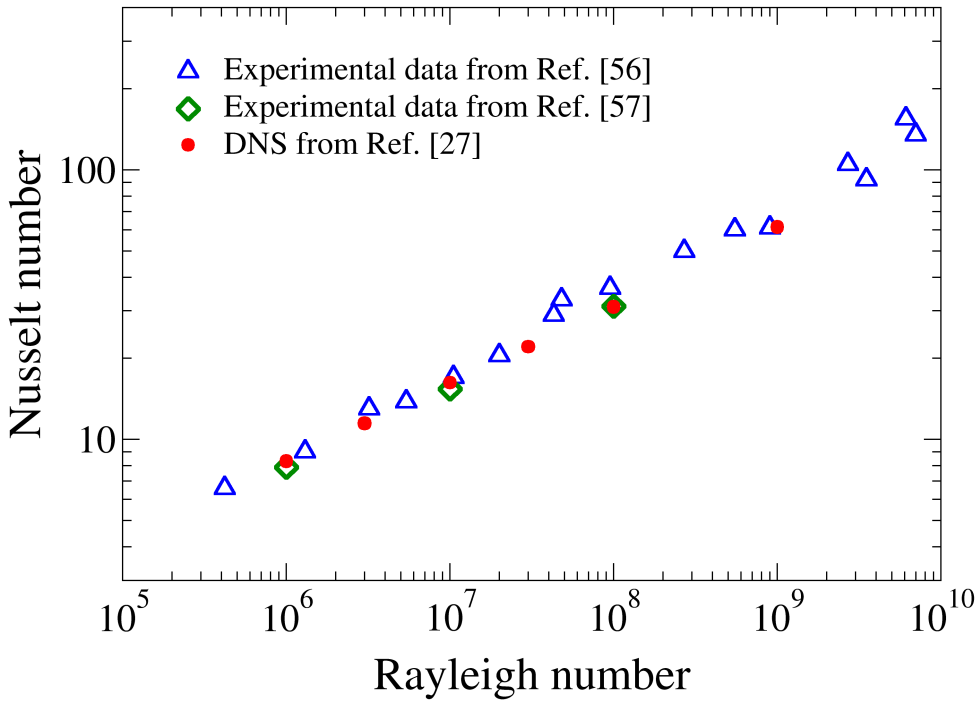

Figure 5: Comparisons between DNS results and experimental data in the case of Rayleigh-Bénard convection in cubical cavities filled with gases. The experimental data are from Belmonte et al [56] with nearly insulated side-walls, and from Leong et al [57] with conducting side-walls. The DNS data correspond to perfectly insulated side-walls [27].

Mesh	M	ϵ	$\theta \times 10^2$	$k^*_{kin} \times 10^4$	$k^*_{tur} \times 10^4$	Nu_{up}	Nu_{left}	Nu_{sides}
DNS	N	0	5.760	2.540	2.710	-14.755	4.968	6.825
LES_{240}	$3N/4$	$1/(4N)$	5.610	2.638	2.998	-15.605	5.381	6.961
LES_{160}	$3N/4$	$1/(4N)$	5.350	2.803	2.547	-16.385	5.979	7.219
LES_{160}	$N/2$	$1/(2N)$	5.370	2.865	2.368	-16.385	6.046	7.192

Table 2: Comparison between LES and DNS results (C case in Table 3, February) on the volume-averaged reduced temperature, the volume-averaged dimensionless kinetic energy of mean flow, the volume-averaged dimensionless turbulent kinetic energy and the averaged Nusselt number at the upper ($X = L_X$), left ($Z = 0$) and side ($Y = 0$) walls.

Case	radiation model	solutal buoyancy
CRM	radiating gas (κ_ν from Fig. 3)	considered (β_c from Tab. 1).
CR	radiating gas (κ_ν from Fig. 3)	disregarded ($\beta_c = 0$)
C	transparent gas ($\kappa_\nu = 0$)	disregarded ($\beta_c = 0$)

Table 3: Three considered cases with different levels of simplifications. The CRM model is the full model described in Sec. 3.

field to buoyancy is ignored ($\beta_c = 0$), so that the velocity and temperature fields can be computed without solving the mass conservation equation (6). The C model uses the same simplifying assumption for buoyancy. In addition, the gas is assumed to be transparent ($\kappa_\nu = 0$). The radiative power is thus zero ($\mathcal{P}_{\text{rad}} = 0$), and the radiative transfer equation (10) can be removed from the model. The convection–radiation coupling is thus ignored in model C, but radiative fluxes still exist between the cave walls separated by the transparent atmosphere. This is the model already used in Ref. [24].

5.2. Flow pattern

Figure 6 shows streamlines of the mean velocity field colored by the kinetic energy of the mean flow in the Y mid-plane for the three models listed in Tab. 3. In the C case, flow patterns and convection intensities differ considerably between May and November, as discussed in previous work [24]. The maximum and minimum wall temperatures are the same for both months, but the mean vertical temperature gradient is negative (i.e., unstable) in May and positive (i.e., stable) in November (see Fig.2). This leads to a one-cell flow pattern associated with intense convection in May and a multiple-cell flow pattern associated with weaker convection in November.

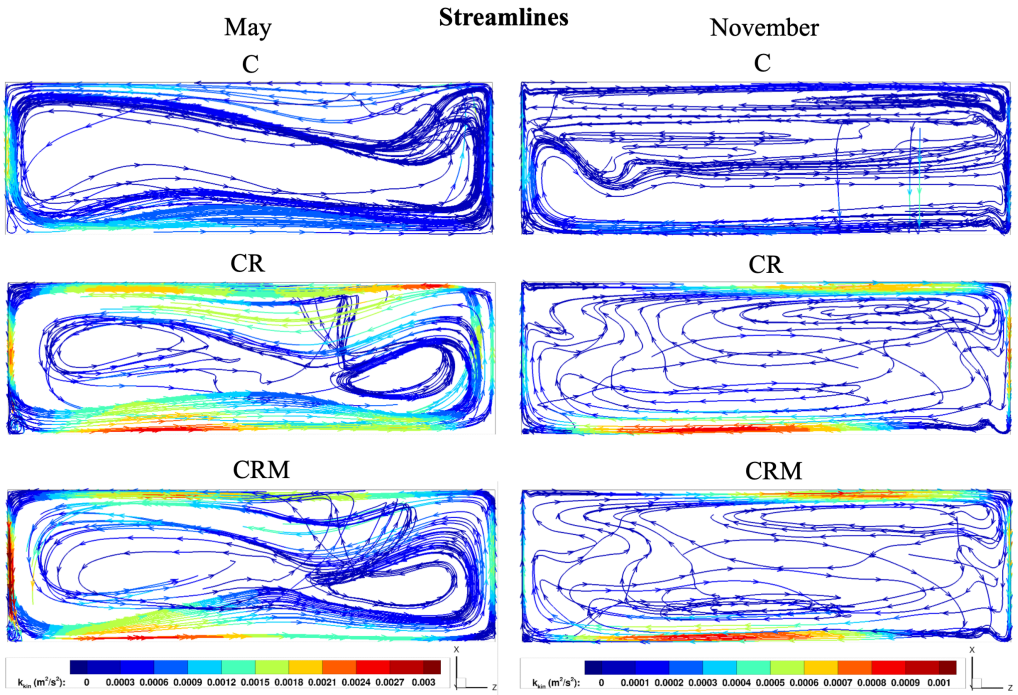

Figure 6: Flow streamlines colored by the kinetic energy of the mean flow for May (left column) and November (right column), for the models C, CR and CRM (see table 3). Streamlines are drawn from the Y mid-plane and then projected onto the Y mid-plane when they deviate from it.

Comparing CR and CRM models for both months, we observe that flow patterns are very similar. This suggests that the solutal buoyancy effect on the flow behavior might be insignificant. Conversely, the gas radiation increases the flow circulation and modifies the streamlines of the mean flow. In May, two secondary cells are observed in the core when the gas radiation is taken into account (CR and CRM cases). In November, gas radiation unsettle the multiple-cell flow pattern observed in case C. Indeed, the flow pattern observed in cases CR and CRM is closer to a one-cell large-scale circulation due to increased kinetic energy of the mean flow, even if two weak secondary cells are noticeable in the upper right and lower regions.

In order to quantify the previous observations, the following macroscopic quantities are reported in Tab. 4: the volume-averaged kinetic energy of the mean flow $k_{kin} = \left\langle \frac{1}{2}\overline{\boldsymbol{u}} \cdot \overline{\boldsymbol{u}} \right\rangle_V$, the volume-averaged turbulent kinetic energy $k_{tur} = \left\langle \frac{1}{2}\overline{\boldsymbol{u}' \cdot \boldsymbol{u}'} \right\rangle_V$ and the maximum of the mean vertical velocity $|\overline{u}|_{\max}$,

May			
	C	CR	CRM
$k_{kin} \times 10^4\,(\mathrm{m}^2/\mathrm{s}^2)$	2.8	6.8	6.9
$k_{tur} \times 10^4\,(\mathrm{m}^2/\mathrm{s}^2)$	0.93	2.7	3.2
$\lvert\overline{u}\rvert_{\max}$ (m/s)	0.095	0.105	0.108
November			
	C	CR	CRM
$k_{kin} \times 10^4\,(\mathrm{m}^2/\mathrm{s}^2)$	0.31	1.1	1.1
$k_{tur} \times 10^4\,(\mathrm{m}^2/\mathrm{s}^2)$	0.066	0.14	0.14
$\lvert\overline{u}\rvert_{\max}$ (m/s)	0.050	0.069	0.069

Table 4: Macroscopic flow quantities

where $\bar{\cdot}$ and $\langle\cdot\rangle_V$ denote time-averaging and volume-averaging, respectively. The comparison between CR and CRM cases confirms the low impact of solutal buoyancy on the flow behavior. Indeed, with the exception of the turbulent kinetic energy k_{kin} which increases by 19 % between CR and CRM models in May, macroscopic quantities are not significantly modified by solutal buoyancy. This weak effect of the moisture gradient on the flow pattern can be readily explained by estimating the order of magnitude of the ratio between the solutal and thermal contributions to buoyancy:

$$\frac{g\beta_c\,(\beta\Delta T)}{g\beta_T\,\Delta T} = \frac{\beta_c\,\beta}{\beta_T} \simeq 0.098 \ll 1\,. \tag{14}$$

The solutal contribution is thus negligible compared to the thermal contribution.

Conversely, the macroscopic quantities in Tab. 4 confirm the thermal convection enhancement due to gas emission and absorption. The kinetic energies k_{kin} and k_{tur} are 2 to 3 times higher in the CR case compared to the C case for both May and November, and $\lvert\overline{u}\rvert_{\max}$ is increased by 11 % in May and by 14 % in November. The gas radiation effect will be discussed in more detail in Sec. 5.3.

5.3. Velocity and thermal fields

Figure 7 displays horizontal profiles of the vertical velocity component and of the temperature close to the left and right walls in the Y mid-plane, at three different heights X, in May. The results from the three models C,

CR and CRM are shown. CR and CRM models yield similar profiles, further confirming the weak solutal buoyancy effect on the flow behavior. The thickness of the fluid layer flowing along the walls is drastically increased due to the change in the temperature distribution induced by gas–wall radiative exchanges. For this month, the gas flows downward along the cold left wall and upward along the hot right wall for the three cases C, CR and CRM (Figs. 7a and 7b). The upward buoyant motion along the right wall is strengthened by the gas radiation as the fluid is heated outside the thermal boundary layer due to the absorption of the wall radiation (black curves in Fig. 7d) resulting in the thickening of the ascending fluid layer. This mechanism of flow enhancement by gas–wall radiative exchanges has been reported in the literature about the differentially heated cavity. It has been evidenced both numerically [30, 31, 32, 33] and experimentally [49].

A similar effect is observed along the left wall where the fluid is cooled in the top left corner due to the emission by the gas (red curves in Fig. 7c). The ascending flow observed at the bottom of this wall (black curves) is due to the presence of a small vortex in the corner (see Fig. 6). Interestingly enough, the inner part of the hydrodynamic and thermal boundary layers (few centimeters thick) is not affected by gas radiation (see Fig. 7). The same trends were observed in November, although the situation is further complicated by the change in the flow pattern induced by gas radiation.

The horizontal velocity component and the temperature profiles along the vertical centerline of the cavity ($Z = L_Z/2$ and $Y = L_Y/2$) are displayed in Fig. 8. As already discussed, the comparison between CRM and CR models does not show any noticeable effect of the solutal buoyancy. Fig. 8a exhibits the intensification of the large-scale counter-clockwise circulation due to the gas radiation effect in May, associated with strong mixing effects resulting in nearly isothermal temperature field in the cavity core (see Fig. 8b, red curves) similar to the profile predicted by the C model. The temperature gradients are confined very close to the walls and are not modified by gas radiation. In November, the multiple-cell regime predicted by the C model is broken by the gas radiation effect (see Fig. 6). The horizontal air motion becomes stronger near the horizontal walls but a part of the core remains almost motionless. We observe a little effect of gas radiation on the vertical temperature profiles (see Fig. 8b, blue curves) but this effect is too weak to significantly modify the thermal stratification obtained with the C model.

Figure 9 presents the vapor concentration profile along the vertical centerline of the cavity. Due to the analogy between heat and mass transfer,

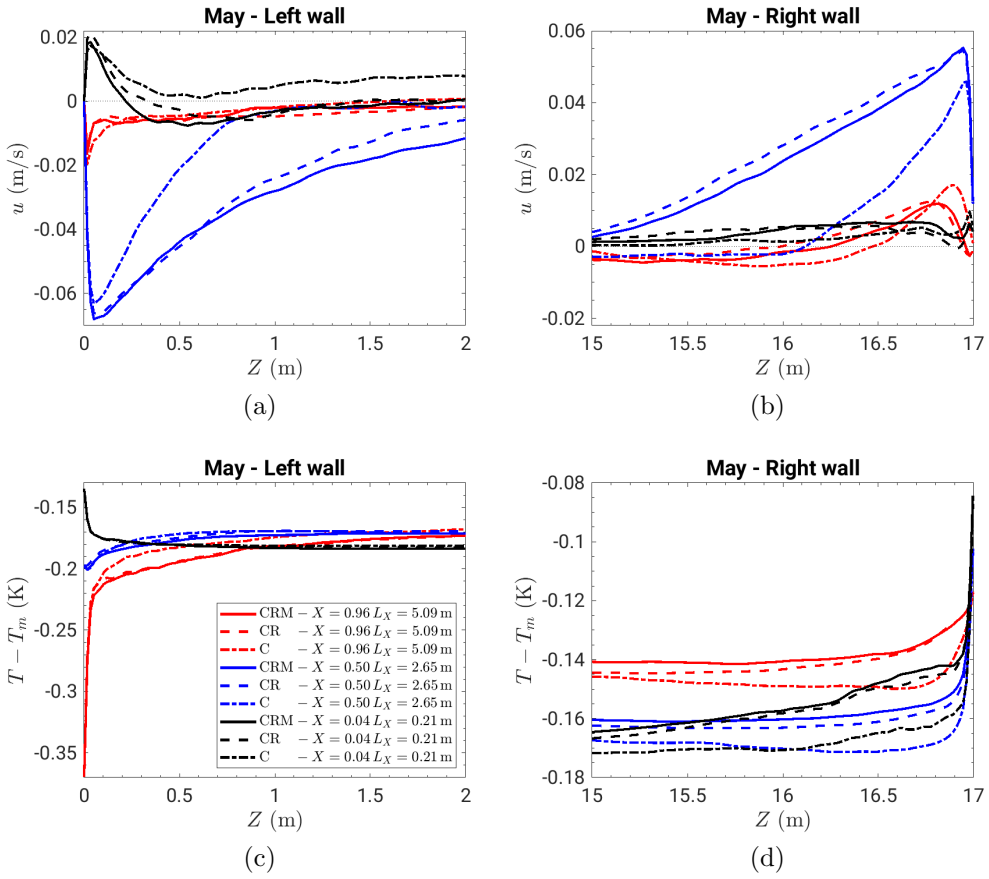

Figure 7: Horizontal profiles of the vertical velocity component u (a) and (b), and of the temperature (c) and (d), in the Y mid-plane at different heights X along the vertical walls for C, CR and CRM models, in May.

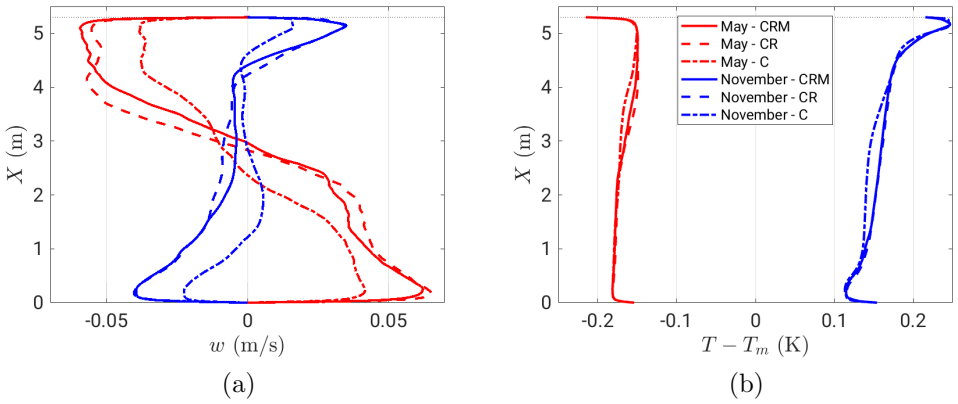

Figure 8: Vertical profiles of the horizontal velocity component W (a) and the temperature (b) along the vertical centerline of the cavity ($Z = L_Z/2$ and $Y = L_Y/2$) for the C, CR and CRM models in May (red curves) and November (blue curves).

the solutal and thermal stratifications are quite similar. However, there is a local non-monotonic variation of the concentration vertical profile in November not observed on the corresponding temperature profile. Because of the homogenization by gas-gas radiative exchanges, the temperature profile is likely less sensitive to the presence of small secondary cells predicted by the CRM model in the core of the cavity in November.

6. Heat and mass transfer through the cavity wall

6.1. Effect of gas radiation on the conductive and radiative fluxes

Figure 10 shows the spatial distribution of the conductive and radiative fluxes along the cavity walls at the mid-plane $Y = L_Y/2$. We checked that CR and CRM models gave indistinguishable results because of the negligible effect of solutal buoyancy (not shown). Differences between the results from C and CRM models is thus due to the presence of gas radiation in the latter case. Despite the strong convection enhancement associated with gas radiation (see Sec. 5.2 and 5.3), the conductive fluxes q_{cond} (blue curves in Fig. 10) are little affected by radiation effects. Gas radiation tends to slightly decrease the conductive flux, but the effect is hardly significant. This is consistent with the temperature profiles displayed in Fig. 7c, 7d and 8b, showing that the wall temperature gradient is not affected by gas radiation.

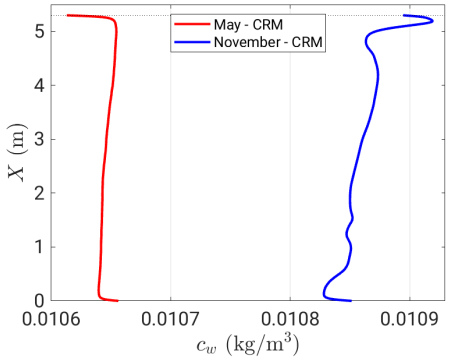

Figure 9: Vapor concentration profile along the vertical centerline of the cavity ($Z = L_Z/2$ and $Y = L_Y/2$) for the CRM model in May and November.

On the other hand, Fig. 10 shows that gas radiation significantly modifies the distribution of the radiative flux q_{rad} along the walls (red curves). The absolute value of the wall radiative flux is rather decreased by gas radiation along the top and bottom walls mainly due to a screening effect. For the left and right walls, the flux is rather increased but the analysis is made difficult by the complex structure of the temperature field in front of these walls.

The effect of gas radiation can go up to a factor two, leaving the order of magnitude of the wall radiative flux unchanged. This result is consistent with the value of the transmissivity $\tau_g \simeq 0.7$ found in Sec. 2.3. The cavity of approximately 10 m length is at the transition between the regimes dominated by wall–to–wall radiation ($\tau_g \simeq 1$) and gas–wall radiation ($\tau_g \ll 1$). This behavior would likely be different in a larger cavity, with a characteristic length of a few tens of meters.

6.2. Energy balance at the cavity wall

The total heat flux q_{th} through the cave walls can be broken down into three terms: the conductive flux q_{con}, the radiative flux q_{rad} and the latent heat flux q_{lat} (see Eq. (12)). In this section, we analyze the relative significance of these three contributions in the energy balance.

6.2.1. Approximate expressions of the mass and latent heat fluxes in CR and C models

Although the solutal contribution to buoyancy is ignored in models C and CR, solving the mass conservation Eq. (6) with the Dirichlet boundary

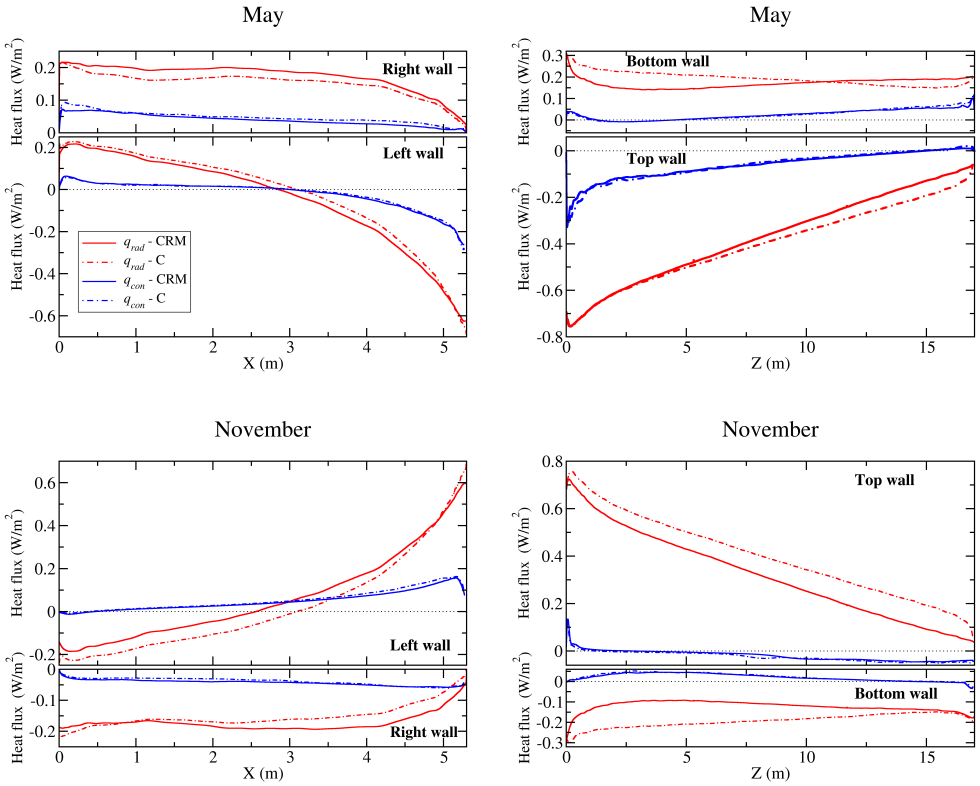

Figure 10: Spatial distribution of conductive (blue lines) and radiative (red lines) heat fluxes at the mid-plane $Y = L_Y/2$ along the left ($Z = 0$), right ($Z = L_Z$), bottom ($X = 0$) and top ($X = L_X$) walls, computed from the CRM and C models in May and November.

condition Eq. (7) is required to get the mass flux $\rho_w v_{ev}$ and the latent heat flux $q_{lat} = \mathcal{L}\rho_w v_{ev}$ through the cavity wall. However, this resolution can be avoided using an approximate solution based on the analogy between heat and mass transfer. With the following assumptions:

1. c_{sat} varies linearly with the gas temperature T,
2. the solutal and thermal diffusivities are equal (i.e., Le = 1),
3. the conductive flux through the cavity wall is not modified by gas radiation,

the dimensionless conductive and mass fluxes through the cavity wall, respectively the Nusselt number $\mathrm{Nu} = q_{con} L_X/(\lambda \Delta T)$ and the Sherwood number $\mathrm{Sh} = \rho_w v_{ev} L_X/(D\beta\Delta T)$, would be equal. The assumptions 1 and 2 above are generally valid in caves, because small temperature variations allow the linearization of $c_{sat}(T)$ and $\mathrm{Le} \sim 1$ is a general property of gases. The assumption 3 is expected to be valid in cavities where radiative transfer is not dominated by gas radiation, i.e., cavities for which the relation $\tau_g \sim 1$ is satisfied. For the specific cavity studied in this work, the assumption 3 has been evidenced in Sec. 6.1, and the relation $\mathrm{Nu} \simeq \mathrm{Sh}$ is confirmed in Fig. 11. It yields:

$$\rho_w v_{ev} = \left(\frac{D\beta}{\lambda}\right) q_{con} \quad \text{and} \quad q_{lat} = \left(\mathcal{L}\frac{D\beta}{\lambda}\right) q_{con} \simeq 1.7\, q_{con}\,. \tag{15}$$

These relations allow to compute the mass flux $\rho_w v_{ev}$ and the latent heat flux q_{lat} from the conductive flux q_{con} and the physical properties of the cave atmosphere. They have been already used by Dreybrodt and Gabrovšek [11] to assess the order of magnitude of condensation fluxes in caves through simple models.

6.2.2. Relative contribution of conductive, radiative and latent heat fluxes to the total flux

We showed in a previous work that conduction was mainly dominated by radiative fluxes between the walls of the cavity filled with a dry and transparent atmosphere [24]. This remains true for the wet and radiant atmosphere considered in this work because: (1) the solutal buoyancy has a negligible effect on the flow, (2) gas radiation hardly changes the conductive flux and does not modify the order of magnitude of the radiative flux (see Sec. 6.1). Indeed, one can check in Fig. 10 that, with the exception of limited

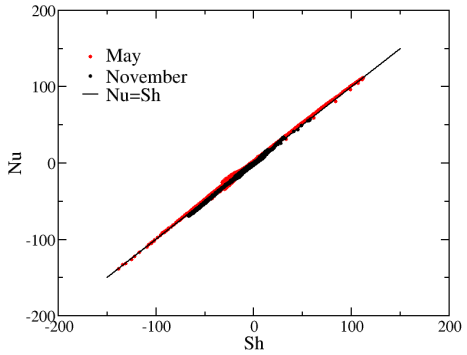

Figure 11: Cloud of points representing the local Nusselt number versus the local Sherwood number for May and November for the CRM model. Each point corresponds to a given spatial location on the wall.

areas where both q_{rad} and q_{con} go to zero, $|q_{rad}/q_{con}| \gtrsim 1$ over the whole cavity surface. More precisely, $1 \lesssim |q_{rad}/q_{con}| \lesssim 3$ in May at the upper left edge (intersection of top and left walls) or at the right of the bottom wall, and in November at the upper right edge (intersection of the top and right walls) and on a part of the bottom wall. $|q_{rad}/q_{con}| \gtrsim 3$ everywhere else.

The latent heat flux q_{lat} must also be considered in the energy balance. Eq. (15) yields $(q_{con} + q_{lat}) \simeq 2.7\, q_{con}$. The added conduction and phase change contributions, both driven by convection, are comparable with the radiation contribution in many places on the walls, and dominate heat transfer in the areas such that $|q_{rad}/q_{con}| \lesssim 3$. The full spatial distribution of the total heat flux q_{th} and its components q_{con}, q_{lat} and q_{rad} are shown in Fig. 12 for the CRM model in May. It is noteworthy that the contribution of convection $(q_{con} + q_{lat})$ is comparable to that of radiation at the upper left edge, where the heat transfer is most intense. The same remark applies in November (not shown).

The wall temperature used in boundary conditions (Eq. (7)) were determined by a large scale model including heat conduction in the rock mass. In this model, the contribution of convection to the energy balance at the cavity walls was assumed negligible with respect to radiation. We see that this assumption fails when humid air is considered. With the addition of the conduction and latent heat fluxes, convection significantly contributes to the heat transfer at the walls. In the configuration studied here, the convection contribution does not exceed radiation, so that the orders of magnitude of

the fluxes should be correctly predicted. However, a full coupling between conduction in the rock and convection inside the cavity should be considered to get an accurate solution in the case of humid air. The feasibility of such simulations will be discussed in the conclusion.

6.3. Mass flux through the cavity wall and consequences on corrosion

As stated in the introduction, condensation and evaporation are of primary interest for the conservation of painted caves. Condensation results in wall corrosion by limestone dissolution. Conversely, evaporation induces limestone deposition. The retreat velocity of the wall v_{ret} is defined as the volume of dissolved limestone per unit of surface and time ($v_{ret} < 0$ indicates limestone deposition).

The evaporation velocity fields on the cave walls are displayed in Fig. 13 for May and November. In May, condensation takes place on the upper left walls, over 43 % of the cavity surface. The maximum condensation rate reaches $18\,\mu$m/day at the upper left edge, where the distance from the ground surface is the shortest (see Fig. 1). The evaporation rate culminates at $6\,\mu$m/day at the lower right edge. The situation is reversed in November. In this case, evaporation takes place on the upper left walls over 41 % of the cavity surface. The maximum rate is $9\,\mu$m/day. Condensation is observed on the lower right walls, with a maximum rate of $3\,\mu$m/day. In May, the negative (unstable) vertical temperature gradient enhances convection, resulting in maximum condensation or evaporation rates multiplied by two compared to November, which is associated with positive (stable) vertical temperature gradient. Therefore, during a full year, there will be more condensation than evaporation in the upper left part of the cave, and the opposite in the lower right part.

The retreat velocity of the wall can be easily deduced from the evaporation velocity. The dissolution of 1 mol of $CaCO_3$ yields 1 mol of ions Ca^{2+} in solution. The concentration of ions Ca^{2+} in a water solution in equilibrium with $CaCO_3$ and a gas phase including CO_2 at partial pressure P_{CO_2} is given by

$$[\mathrm{Ca}^{2+}] \simeq \mathcal{K}\, P_{CO_2}^{1/3} \tag{16}$$

where the parameter $\mathcal{K}$ can be computed from the equilibrium constants of the system $H_2O/CO_2/CaCO_3$ [50]. Using the data from Ref. [51], we get $\mathcal{K} \simeq 8.27\,\mathrm{mmol.L^{-1}.atm^{-1/3}}$ at 12°C ($CaCO_3$ in calcite form). Dreybrodt and Gabrovšek [11] showed that the thin film of condensed water lying on a

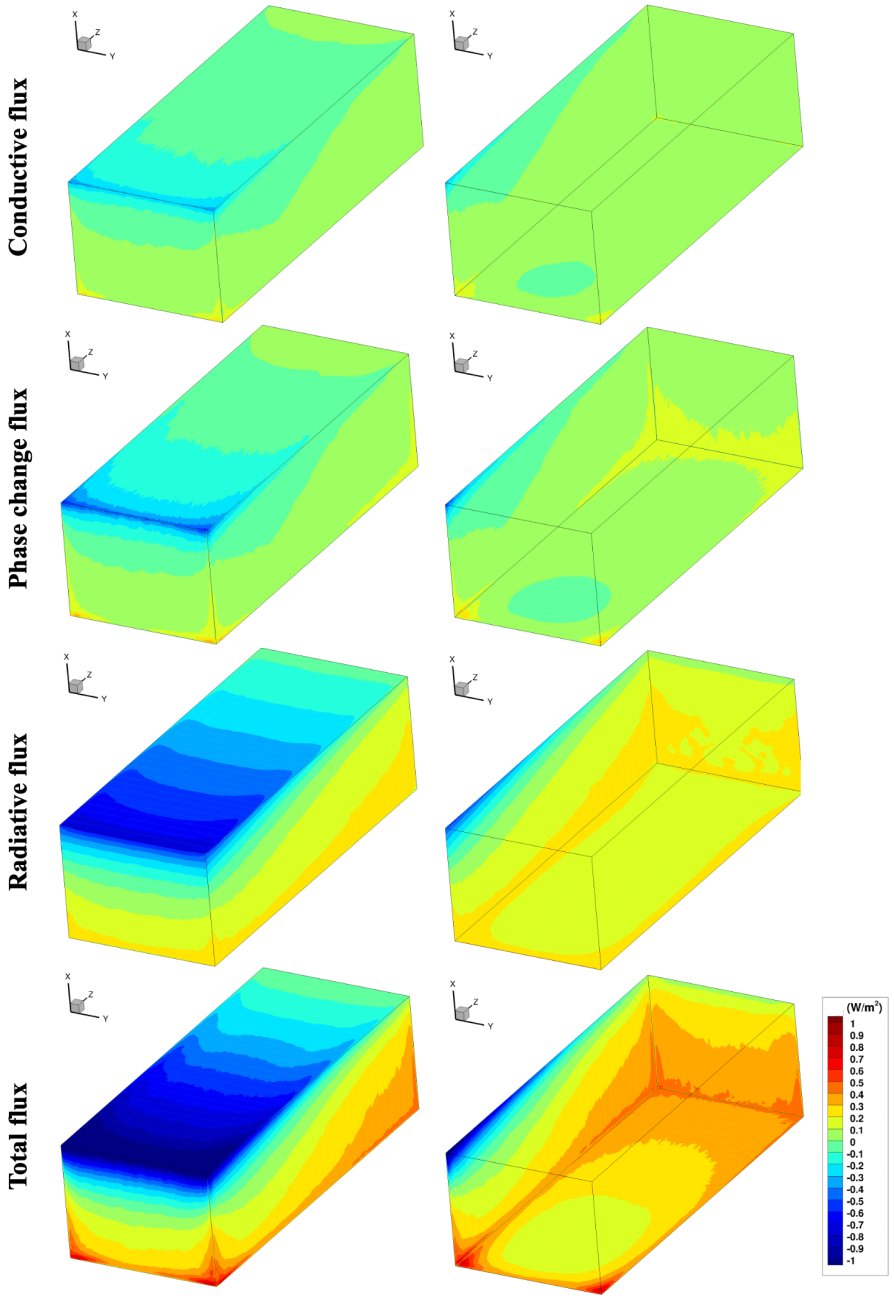

Figure 12: Spatial distribution of conductive (q_{con}), water phase change (q_{lat}), radiative (q_{rad}) and total (q_{th}) wall heat fluxes for the CRM model in May. The left panel corresponds to the top ($X = L_X$), left ($Z = 0$) and front ($Y = L_Y$) cave walls. The right panel corresponds to the bottom ($X = 0$), right ($Z = L_Z$) and rear ($Y = 0$) cave walls.

limestone wall can be regarded as saturated with respect to limestone and CO_2. They came to this conclusion after performing a series of laboratory experiments covering wide ranges of condensation rates and CO_2 partial pressure commonly found in nature. The retreat velocity can thus be deduced from Eq. (16) along with mass conservation:

$$v_{ret} = -\frac{\mathcal{K}\mathcal{M}}{\rho_c}\, P_{CO_2}^{1/3}\, v_{ev} \tag{17}$$

where $\mathcal{M} \simeq 100\,\mathrm{g/mol}$ and $\rho_c \simeq 2700\,\mathrm{kg/m^3}$ are the molar mass and the density of $CaCO_3$, respectively. The value $P_{CO_2} = x_{CO_2}\, P_{atm} = 0.02\,\mathrm{atm}$ is considered in the following.

The behavior of the retreat velocity v_{ret} can be directly deduced from the evaporation velocity v_{ev}, since both velocities are proportional. The upper left edge undergoes corrosion in May and deposition in November, with retreat velocities reaching respectively 0.55 and $-0.27\,\mu$m/year. Conversely, the lower right edge undergoes evaporation in May and condensation in November, with retreat velocities of -0.18 and $0.09\,\mu$m/year, respectively. Therefore, over a full year, dissolution dominates in the upper left region, and deposition in the lower right region.

There are few studies in the literature providing quantitative measurements of condensation or evaporation rates in caves. In the Glowworm cave (New Zealand), when the cave entrance was closed to prevent air circulation, De Freitas and Schmekal [52] measured condensation and evaporation rates oscillating from 0 to approximately $10\,\mu$m/day. Buecher [53] measured evaporation rates in Kartchen Caverns (Arizona), a wet cave with water percolating from the surface, little air exchange with the outside, and thus high relative humidity (over 99%). The average evaporation rate for all stations installed in the cave was $10\,\mu$m/day, reduced to $6\,\mu$m/day for stations far from the entrance. The orders of magnitude predicted by our numerical simulations (a few microns per day) are in line with these values. Condensation rates higher by an order of magnitude were reported in the literature (see Ref. [54]), but in configurations far from the one studied in this article (high–ventilated areas or hydrothermal caves). Corrosion induced by condensation was also investigated. Cailhol *et al* [55] found from a literature review that the retreat velocity in a limestone cave should be in the range from 0.3 to $30\,\mu$m/year. Our estimation for a weakly ventilated cave (a few tenths of a micron per year) falls in the lower part of this range.

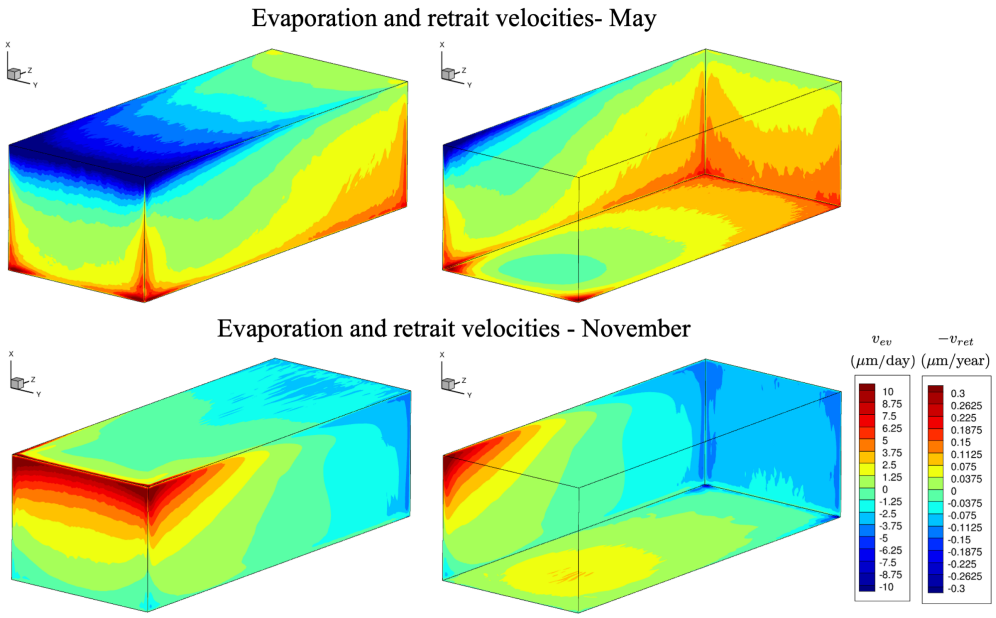

Figure 13: Spatial distribution of the evaporation velocity v_{ev} and the retreat velocity v_{ret} from the CRM model in May and November. v_{ret} is proportional to v_{ev} [from Eq.(17): $v_{ret}/(\mu\text{m/year}) \simeq -0.030\, v_{ev}/(\mu\text{m/day})$]. The left panel corresponds to the top ($X = L_X$), left ($Z = 0$) and front ($Y = L_Y$) cave walls. The right panel corresponds to the bottom ($X = 0$), right ($Z = L_Z$) and rear ($Y = 0$) cave walls.

7. Conclusion

A major outcome of the numerical simulations is the strong similarities between the results obtained in the shallow cave considered in this study and in the classical differentially heated cavity, despite the simplicity of the thermal boundary conditions in the latter case (two isothermal vertical parallel walls surrounded by adiabatic walls). In a shallow cave, opposite vertical and horizontal walls at different distances from the ground surface have different non-uniform temperatures. Due to buoyancy forces, the hot and cold vertical walls classically drive the air flow upward and downward, respectively, inducing a global circulation in the cavity. Convection is enhanced when the vertical temperature gradient is negative, i.e., when the floor is warmer than the ceiling.

Heat and mass fluxes are maximum in areas of the cavity roof where the distance from the ground is the shortest. Due to the asymmetry induced by the inversion of the vertical temperature gradient twice a year, net condensation/corrosion is expected in these areas, whereas the other regions of the cave undergo net evaporation/deposition. The orders of magnitude of the condensation flux (a few microns per day) and of the retreat velocity (a few tenth of a micron per year) are in line with the field data available in the literature.

Gas radiation increases the flow circulation in the cavity through wall–gas radiative exchanges. This results in a higher stirring of the cavity core, but the wall conduction and mass fluxes are not modified. This effect was already observed in the differentially heated cavity. In contrast, gas radiation significantly modifies the wall radiative flux, but without changing its order of magnitude. This is consistent with the estimation of the transmissivity ($\tau_g \simeq 0.7$) based on the cavity size (approximately 10 m). A transmissivity slightly lower than 1 indicates a transition between the regimes dominated by surface radiation and gas radiation. Gas radiation should be clearly dominant for larger cavities (typically a few tens of meters).

The contribution of the water concentration gradient to buoyancy can be neglected compared to the temperature contribution. However, the heat flux released by the latent heat of evaporation or condensation must be considered in the energy balance at the wall. Indeed, the addition of the latent heat and conduction fluxes, both driven by convection, prevails over radiation in some regions of the cavity. Therefore, more accurate predictions of heat and mass fluxes at the cavity walls require to couple natural convection inside the

cavity with conduction in the rock mass. Although the present Large-Eddy Simulations are computationally expensive, this coupling should be feasible given the large time scale associated with the conduction in the rock allowing low coupling frequencies. A last limitation of this study is the cave geometry that is not representative of actual caves. Considering realistic geometries and unstructured meshes would increase the computational time required for the flow simulation but associated numerical methods (finite element, finite-volume) would benefit from a much more efficient parallel implementation than our spectral algorithm.

Acknowledgements

This work was funded by the financial support of the LabeX LaSIPS (ANR-10-LABX-0032-LaSIPS) managed by the French National Research Agency under the "Investissements d'avenir" program (ANR-11-IDEX-0003-02). This work was granted access to the HPC resources of IDRIS under the allocation 2021- A0102B00209 attributed by GENCI (Grand Equipement National de Calcul Intensif). This work was also performed using HPC resources from the "Mésocentre" computing center of CentraleSupélec and École Normale Supérieure Paris-Saclay supported by CNRS and Région Île-de-France (http://mesocentre.centralesupelec.fr/).

References

[1] M. Cuthbert, G. Rau, M. Andersen, H. Roshan, H. Rutlidge, C. Marjo, M. Markowska, C. Jex, P. Graham, G. Mariethoz, R. Acworth, A. Baker, Evaporative cooling of speleothem drip water, Sci. Rep. 4 (2014) 5162.

[2] Y. Lv, Y. Jiang, W. Hu, M. Cao, Y. Mao, A review of the effects of tunnel excavation on the hydrology, ecology, and environment in karst areas: Current status, challenges, and perspectives, J. Hydrogeol. 586 (2020) 124891.

[3] D. C. Culver, T. Pipan, The biology of caves and other subterranean habitats, Oxford University Press, 2009.

[4] P. L. Fernández, I. Gutierrez, L. S. Quindós, J. Soto, E. Villar, Natural ventilation of the paintings room in the Altamira Cave, Nature 321 (1986) 586–588.

[5] A. A. Cigna, Environmental management of tourist caves, Environ. Geol. 21 (1993) 173–180.

[6] S. Sánchez-Moral, V. Soler, J. Cañaveras, E. Sanz-Rubio, R. Van Grieken, K. Gysels, Inorganic deterioration affecting the Altamira Cave, N Spain: quantitative approach to wall-corrosion (solutional etching) processes induced by visitors, Sci. Total Environ. 243-244 (1999) 67–84.

[7] J. Brunet, J. Vouvé, P. Malaurent, Re-establishing an underground climate appropriate for the conservation of the prehistoric paintings and engravings at Lascaux, Conserv. Manage. Archaeol. Sites 4 (2000) 33–45.

[8] F. Bourges, P. Genthon, D. Genty, M. Lorblanchet, E. Mauduit, D. D'Hulst, Conservation of prehistoric caves and stability of their inner climate: Lessons from Chauvet and other French caves, Sci. Total Environ. 493 (2014) 79–91.

[9] P. M. Martin-Sanchez, A. Z. Miller, C. Saiz-Jimenez, Lascaux Cave: An example of fragile ecological balance in subterranean environments, in: E. A. Summers (Ed.), Microbial life of cave systems, De Gruyter, 2015, Ch. 13, pp. 279–301.

[10] R. F. Tarhule-Lips, D. C. Ford, Condensation corrosion in caves on Cayman Brac and Isla des Mona, J. Cave Karst Studies 60 (1998) 84–95.

[11] W. Dreybrodt, F. Gabrovšek, M. Perne, Condensation corrosion: a theoretical approach, Acta carsologica 34 (2005) 317–348.

[12] P. Malaurent, J. Brunet, D. Lacanette, J.-P. Caltagirone, Contribution of numerical modelling of environmental parameters to the conservation of prehistoric cave paintings: the example of Lascaux Cave, Conserv. Manage. Archaeol. Sites 8 (2007) 59–76.

[13] L. Laiz, J. Gonzalez, C. Saiz-Jimenez, Microbial communities in caves: ecology, physiology, and effects on Paleolithic paintings, Art, biology, and conservation: Biodeterioration of works of art (2003) 210–225.

[14] Y. Li, D. Ogura, S. Hokoi, J. Wang, T. Ishizaki, Predicting hygrothermal behavior of an underground stone chamber with 3-D modeling to restrain

water-related damage to mural paintings, Journal of Asian Architecture and Building Engineering 13 (2014) 499–506.

[15] J. Martin, F. Doumenc, Condensation–induced self–patterning of a thin clayey layer, EPL 138 (2022) 13001.

[16] A. Bini, M. Cavalli Gori, G. S., A critical review of hypotheses on the origin of vermiculations, Int. J. Speleol. 10 (1978) 11–33.

[17] S. Hœrlé, S. Konik, É. Chalmin, Les vermiculations de la grotte de lascaux : identification de sources de matériaux mobilisables par micro-analyses physico-chimiques, Karstologia 58 (2011) 29–40.

[18] J. Clottes, Midi-Pyrénées, Gallia Préhistoire 24 (2) (1981) 525–570.

[19] L. S. Quindos, A. Bonet, N. Diaz-Caneja, P. L. Fernandez, I. Gutierrez, J. R. Solana, J. Soto, E. Villar, Study of the environmental variables affecting the natural preservation of the Altamira Cave paintings located at Santillana del Mar, Spain, Atmos. Environ. 21 (1987) 551–560.

[20] E. Villar, P. L. Fernández, L. S. Quindós, J. R. Solana, J. Soto, Temperature of rock surfaces in Altamira Cave (Spain), Cave Sci. 10 (1983) 165–170.

[21] N. Houillon, R. Lastennet, A. Denis, P. Malaurent, S. Minvielle, N. Peyraube, Assessing cave internal aerology in understanding carbon dioxide (CO_2) dynamics: implications on calcite mass variation on the wall of Lascaux Cave (France), Environ. Earth Sci. 76 (2017) 170.

[22] B. Guerrier, F. Doumenc, A. Roux, S. Mergui, P.-Y. Jeannin, Climatology in shallow caves with negligible ventilation: heat and mass transfer, Int. J. Therm. Sci. 146 (2019) 106066.

[23] N. Houillon, La dynamique du carbone inorganique dans le continuum sol-épikarstique-cavité du site de la grotte de Lascaux (France), Ph.D. thesis, University of Bordeaux (2016).

[24] B. Qaddah, L. Soucasse, F. Doumenc, S. Mergui, P. Rivière, A. Soufiani, Influence of turbulent natural convection on heat transfer in shallow caves, Int. J. Therm. Sci. 177 (2022) 107524.

[25] P.-Y. Jeannin, M. Hessenauer, A. Malard, V. Chapuis, Impact of global change on Karst groundwater mineralization in the Jura mountains, Sci. Total Environ. 541 (2016) 1208–1221.

[26] Y. Wang, A. Sergent, D. Saury, D. Lemonnier, P. Joubert, Numerical study of an unsteady confined thermal plume under the influence of gas radiation, Int. J. Therm. Sci. 156 (2020) 106474.

[27] M. Delort-Laval, L. Soucasse, P. Rivière, A. Soufiani, Rayleigh–Bénard convection in a cubic cell under the effects of gas radiation up to Ra=10^9, Int. J. Heat Mass Transfer 187 (2022) 122453.

[28] K. Lari, M. Baneshi, S. A. Gandjalikhan Nassab, A. Komiya, S. Maruyama, Combined heat transfer of radiation and natural convection in a square cavity containing participating gases, Int. J. Heat Mass Transfer 54 (2011) 5087–5099.

[29] Y. Billaud, D. Saury, D. Lemonnier, Numerical investigation of coupled natural convection and radiation in a differentially heated cubic cavity filled with humid air. Effects of the cavity size., Numer. Heat Transfer, Part A 72 (2017) 495–518.

[30] L. Soucasse, Ph. Rivière, A. Soufiani, S. Xin, P. Le Quéré, Transitional regimes of natural convection in a differentially heated cavity under the effects of wall and molecular gas radiation, Physics of Fluids 26 (2014) 024105.

[31] L. Soucasse, Ph. Rivière, A. Soufiani, Natural convection in a differentially heated cubical cavity under the effects of wall and molecular gas radiation at Rayleigh numbers up to $3\times$ 10^9, Int. J. Heat Fluid Flow 61-B (2016) 510–530.

[32] T. Kogawa, J. Okajima, A. Sakurai, A. Komiya, S. Maruyama, Influence of radiation effect on turbulent natural convection in cubic cavity at normal temperature atmospheric gas, Int. J. Heat Mass Transfer 104 (2017) 456–466.

[33] T. Kogawa, L. Chen, J. Okajima, A. Sakurai, A. Komiya, S. Maruyama, Effects of concentration of participating media on turbulent natural convection in cubic cavity, Appl. Therm. Eng. 131 (2018) 141–149.

[34] N. Peyraube, R. Lastennet, A. Denis, P. Malaurent, N. Houillon, J.-D. Villanueva, Determination and quantification of major climatic parameters influencing the CO_2 of Lascaux Cave, Theor. Appl. Climatol. 133 (2018) 1291–1301.

[35] G. Badino, Clouds in caves, Speleogenesis and evolution of karst aquifer 2 (2004) 1–8.

[36] J. Dredge, I. Fairchild, R. Harrison, A. Fernandez-Cortes, S. Sanchez-Moral, V. Jurado, J. Gunn, A. Smith, C. Spötl, D. Mattey, P. Wynn, N. Grassineau, Cave aerosols: distribution and contribution to speleothem geochemistry, Quat. Sci. Rev. 63 (2013) 23–41.

[37] G. Barnes, The effect of monolayers on the evaporation of liquids, Advances in colloid and interface science 25 (1986) 89–202.

[38] I. Gordon, L. Rothman, C. Hill, R. Kochanov, Y. Tan, P. Bernath, M. Birk, V. Boudon, A. Campargue, K. Chance, B. Drouin, J.-M. Flaud, R. Gamache, J. Hodges, D. Jacquemart, V. Perevalov, A. Perrin, K. Shine, M.-A. Smith, J. Tennyson, G. Toon, H. Tran, V. Tyuterev, A. Barbe, A. Császár, V. Devi, T. Furtenbacher, J. Harrison, J.-M. Hartmann, A. Jolly, T. Johnson, T. Karman, I. Kleiner, A. Kyuberis, J. Loos, O. Lyulin, S. Massie, S. Mikhailenko, N. Moazzen-Ahmadi, H. Müller, O. Naumenko, A. Nikitin, O. Polyansky, M. Rey, M. Rotger, S. Sharpe, K. Sung, E. Starikova, S. Tashkun, J. V. Auwera, G. Wagner, J. Wilzewski, P. Wcisło, S. Yu, E. Zak, The HITRAN2016 molecular spectroscopic database, Journal of Quantitative Spectroscopy and Radiative Transfer 203 (2017) 3–69, HITRAN2016 Special Issue. doi:https://doi.org/10.1016/j.jqsrt.2017.06.038.
URL https://www.sciencedirect.com/science/article/pii/S0022407317301073

[39] W. Rohsenow, J. Hartnett, Y. Cho, Handbook of heat transfer, McGraw-Hill (1998).

[40] S. Xin, P. Le Quéré, An extended Chebyshev pseudo-spectral benchmark for the 8:1 differentially heated cavity, Numerical Methods in Fluids 40 (2002) 981–998.

[41] S. Xin, J. Chergui, P. Le Quéré, 3D spectral parallel multi-domain computing for natural convection flows, in: Springer (Ed.), Parallel Compu-

885 tational Fluid Dynamics, Lecture Notes in Computational Science and
886 Engineering book series, Vol. 74, 2008, pp. 163–171.

887 [42] E. Tadmor, Convergence of spectral methods for nonlinear conservation
888 laws, SIAM J. Numer. Anal. 26 (1) (1989) 30–44.

889 [43] G. S. Karamanos, G. E. Karniadakis, A spectral vanishing viscosity
890 method for large-eddy simulations, Journal of Computational Physics
891 163 (2000) 22–50.

892 [44] R. Pasquetti, Spectral vanishing viscosity method for large-eddy sim-
893 ulation of turbulent flows, Journal of Scientific Computing 27 (2006)
894 365–375.

895 [45] L. Pierrot, P. Rivière, A. Soufiani, J. Taine, A fictitious-gas-based ab-
896 sorption distribution function global model for radiative transfer in hot
897 gases, Journal of Quantitative Spectroscopy and Radiative Transfer 62
898 (1999) 609–624.

899 [46] L. Soucasse, Ph. Rivière, S. Xin, P. Le Quéré, A. Soufiani, Numerical
900 study of coupled molecular gas radiation and natural convection in a
901 differentially heated cubical cavity, Comput. Therm. Sci. 4 (2012) 335–
902 350.

903 [47] L. Soucasse, Ph. Rivière, A. Soufiani, Subgrid-scale model for radia-
904 tive transfer in turbulent participating media, Journal of Computational
905 Physics 257, Part A (2014) 442–459.

906 [48] L. Soucasse, B. Podvin, Ph. Rivière, A. Soufiani, Low-order models for
907 predicting radiative transfer effects on Rayleigh-Bénard convection in a
908 cubic cell at different rayleigh numbers, Journal of Fluid Mechanics 917
909 (2021) A5.

910 [49] T. Kogawa, E. Shoji, J. Okajima, A. Komiya, S. Maruyama, Experimen-
911 tal evaluation of thermal radiation effects on natural convection with a
912 rayleigh number of $10^8 - 10^9$ by using an interferometer, Int. J. Heat
913 Mass Transfer 132 (2019) 1239–1249.

914 [50] W. White, Chemistry and karst, Acta Carsologica 440 (2015) 349–362.

[51] B. Lopez, Les processus de transfert d'eau et de dioxyde de carbone dans l'épikarst, Ph.D. thesis, Université Bordeaux 1 (2009).

[52] C. R. de Freitas, A. Schmekal, Studies of condensation/evaporation process in the Glowworm Cave, New Zealand, Int. J. Speleol. 35 (2006) 75–81.

[53] R. Buecher, Pre-development studies at Kartchner Caverns, in: National Cave Management Symposium Proceedings, Bowling Green, Kentucky, 1991, pp. 144–163.

[54] V. N. Dublyansky, Y. V. Dublyansky, The problem of condensation in karst studies, J. Cave Karst Studies 60 (1998) 3–17.

[55] D. Cailhol, P. Audra, C. Nehme, F. H. Nader, M. Garašic, V. Heresanu, S. Gucel, I. Charalambidou, L. Satterfield, H. Cheng, R. L. Edwards, The contribution of condensation–corrosion in the morphological evolution of caves in semi-arid regions: preliminary investigations in the Kyrenia Range, Cyprus, Acta Carsologica 48 (2019) 5–27.

[56] A. Belmonte, A. Tilgner, and A. Libchaber, Temperature and velocity boundary layers in turbulent convection, Phys. Rev. E, 50 (1994) 269–279.

[57] W.H. Leong, K.G.T. Hollands, and A.P. Brunger, Experimental Nusselt numbers for a cubical-cavity benchmark problem in natural convection, Int. J. Heat Mass Transfer, 42 (1999) 1979–1989.

[58] L. Soucasse, Effets des transferts radiatifs sur les écoulements de convection naturelle dans une cavité différentiellement chauffée en régimes transitionnel et faiblement turbulent, PhD thesis, École Centrale Paris, France, 2013.